Title

Structure-guided simulations illuminate the mechanism of ATP transport through VDAC1

Permalink

https://escholarship.org/uc/item/83p0q4z9

Journal

Nature Structural & Molecular Biology, 21(7)

ISSN

1545-9993

Authors

Choudhary, Om P
Paz, Aviv
Adelman, Joshua L
et al.

Publication Date

2014-07-01

DOI

10.1038/nsmb.2841

nature
structural &
molecular biology

Structure-guided simulations illuminate the mechanism of ATP transport through VDAC1

Om P Choudhary[1,9], Aviv Paz[2,9], Joshua L Adelman[3,9], Jacques-Philippe Colletier[4–6,9], Jeff Abramson[2,7] & Michael Grabe[3,8]

The voltage-dependent anion channel (VDAC) mediates the flow of metabolites and ions across the outer mitochondrial membrane of all eukaryotic cells. The open channel passes millions of ATP molecules per second, whereas the closed state exhibits no detectable ATP flux. High-resolution structures of VDAC1 revealed a 19-stranded β-barrel with an α-helix partially occupying the central pore. To understand ATP permeation through VDAC, we solved the crystal structure of mouse VDAC1 (mVDAC1) in the presence of ATP, revealing a low-affinity binding site. Guided by these coordinates, we initiated hundreds of molecular dynamics simulations to construct a Markov state model of ATP permeation. These simulations indicate that ATP flows through VDAC through multiple pathways, in agreement with our structural data and experimentally determined physiological rates.

Each day, humans turn over an amount of ATP equivalent to their body weight[1]. The mitochondria are the principal source of ATP generation; therefore, a high number of ATP molecules must exit the mitochondria—primarily through VDACs. In mammals, there are three VDAC isoforms (VDAC1, VDAC2 and VDAC3), which form the main conduits for this large flux of metabolites across the outer membrane from the mitochondrial intermembrane space (IMS) to the cytosol. In addition to their role in bioenergetics, VDACs act as a scaffold, influencing mitochondrial and cellular physiology through interactions with a variety of proteins and small molecules[2–6]. In accordance with these crucial functions, VDACs are expressed in all eukaryotes[7], and knockouts in mice give rise to respiratory defects, embryonic lethality and sterility[8].

Three independent structures of VDAC1 have been reported[9–11], thus providing new insight into the architecture and function of the channel. All structures revealed a 19-stranded β-barrel fold with an N-terminal α-helix in the central pore adjacent to the wall (**Fig. 1**). The channel has a 27-Å-wide opening facing both the cytosol and IMS, but it tapers to 14-Å wide in the center, owing to the presence of the helical segment (**Fig. 1**). In the absence of a membrane potential, VDAC1 adopts a high-conductance (450–580 pS in 100 mM KCl), anion-selective (1.7–1.9 anion-to-cation) state that is capable of passing millions of ATP molecules per second *in vitro*[12] and up to 100,000 ATP molecules per second under physiological conditions[12,13]. Meanwhile, membrane voltages above or below ±30 mV, as well as several other environmental cues, induce a conformation with reduced conductance (220 pS in 100 mM KCl) that is slightly cation selective and lacks detectable ATP flux[12,14,15]. Continuum calculations[16] and atomistic molecular dynamics (MD) simulations[17] have both demonstrated that the solved structures are probably in the open state, because these computations revealed anion selectivity and a high single-channel conductance.

Many biochemical and computational studies have validated these crystal structures; however, some researchers still debate whether they represent a physiologically relevant state. In particular, it has been argued that the transmembrane (TM) topology in the crystal structures is inconsistent with several biochemical and functional studies (reviewed in ref. 18) and that this inconsistency stems from misfolding of the channel during the refolding step of protein purification. On the basis of these later experiments, a model in which VDAC has 13 TM-spanning β-strands and a single TM α-helix as part of the protein's pore has been proposed[8,19]. Yet other researchers contend that the channel radius derived from the high-resolution structures is consistent with that measured from electron micrographs of native VDAC in mitochondrial outer membranes (reviewed in ref. 20). Moreover, early bioinformatics analysis of the primary sequence suggested that the protein has 19 strands[21], in agreement with the three-dimensional structures. Regardless, there are strong arguments from both sides in this debate, and only additional research will resolve the current contradictions in the literature.

Here, we set out to determine whether, and how, the mVDAC1 structure conducts ATP, using a combination of X-ray crystallography

---

[1]Joint Carnegie Mellon University–University of Pittsburgh PhD Program in Computational Biology, Pittsburgh, Pennsylvania, USA. [2]Department of Physiology, David Geffen School of Medicine, University of California, Los Angeles, Los Angeles, California, USA. [3]Department of Biological Sciences, University of Pittsburgh, Pittsburgh, Pennsylvania, USA. [4]Université Grenoble Alpes, Institut de Biologie Structurale, Grenoble, France. [5]Centre National de la Recherche Scientifique, Institut de Biologie Structurale, Grenoble, France. [6]Commissariat à l'Énergie Atomique et aux Énergies Alternatives, Direction des Sciences du Vivant, Institut de Biologie Structurale, Grenoble, France. [7]Institute for Stem Cell Biology and Regenerative Medicine, National Centre for Biological Sciences–Tata Institute of Fundamental Research, Bangalore, India. [8]Cardiovascular Research Institute, Department of Pharmaceutical Chemistry, University of California, San Francisco, San Francisco, California, USA. [9]These authors contributed equally to this work. Correspondence should be addressed to M.G. (michael.grabe@ucsf.edu) or J.A. (jabramson@mednet.ucla.edu).

Received 3 December 2013; accepted 14 May 2014; published online 8 June 2014; doi:10.1038/nsmb.2841

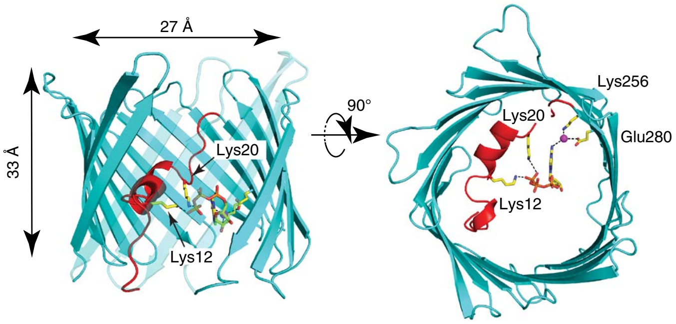

Figure 1 Cartoon representations of the refined mVDAC1 in complex with ATP. mVDAC1 in complex with ATP is shown as viewed from within the plane of the membrane (left) and from the cytosol (right). ATP is bound to mVDAC1 at the center of the pore, forming hydrogen bonds between the side chain nitrogens of residues Lys12 and Lys20 with the O2γ and O1γ of the phosphate tail (2.3 and 3.3 Å, respectively). A structural water (magenta) interacts with the N6 nitrogen on the A ring (N6–water oxygen distance of 3.2 Å), and the water also hydrogen-bonds to Lys256 Nζ and Glu280 Oε2 (distances to water oxygen of 2.7 and 2.9 Å, respectively). The polypeptide chain is in cartoon representation with the β-barrel and the N-terminal α-helix segment colored cyan and red, respectively. All highlighted interactions are indicated by black dashed lines. The side chains and ATP are shown in ball-and-stick representation. To facilitate visualization of ATP, strands 7–10 are partially transparent. The inner-pore dimensions are indicated at the left.

and MD simulations. Our crystal structure of the channel in the presence of ATP uncovers a weak binding site in the pore domain, the location of which is in excellent agreement with earlier MS studies[22] and predictions from our MD simulations. Although MD simulations 1–5 µs long failed to reveal a full ATP passage event, the application of a Markov state model (MSM) of permeation predicts that ATP traverses the channel on a 10- to 50-µs timescale consistent with the channel being in the open state. We used transition path theory analysis to visualize how ATP moves through mVDAC1, and the results indicate that the molecule exploits a number of distinct, interconnected pathways composed of basic, pore-lining residues to cross the channel.

RESULTS

An ATP-binding site identified via X-ray crystallography

Earlier experiments using current fluctuations[23], structure-specific noise generation[24] and MS[22] have demonstrated that ATP weakly interacts with the N-terminal α-helix of VDAC1 as well as with a patch of basic residues on the β-barrel wall. To identify specific binding sites, we undertook the structural characterization of the VDAC–ATP complex by soaking mVDAC1 crystals for 1 h in 50 mM ATP (details on the soaking procedure in Online Methods). Structure determination revealed a lone ATP-binding site, adjacent to the N-terminal α-helix, in which the molecule directly contacts Lys12 and Lys20 (**Fig. 1**). In the refined structure, the side chain nitrogen of Lys12 is 2.3 Å and 3.2 Å from the O2γ and O3β phosphate oxygen atoms, respectively, while the side chain nitrogen of Lys20 is 3.3 Å from O1γ. The importance of Lys20 in ATP binding has also been recently demonstrated for human VDAC1 by NMR[25]. Additionally, we observed that nitrogen N6 from the A ring interacts with a structural water molecule (distance to water oxygen of 3.2 Å), which itself hydrogen-bonds to Lys256 Nζ and Glu280 Oε2 (distances to water oxygen of 2.7 and 2.9 Å, respectively) (**Fig. 1**). Although the presence of extra density at the ATP site was unequivocal on the basis of Fourier difference maps between the ATP-soaked and native data sets, the ATP displayed weak electron density and high *B* factors with a reasonable real-space map correlation of 0.8. This observation is consistent with a low-affinity binding site and suggests that ATP is highly mobile in the pore (further details on structural refinement in Online Methods, **Supplementary Fig. 1** and **Table 1**). Additionally, despite having 50 mM Mg^{2+} in the crystallization conditions, we did not observe clear density for the ion, owing to either the high ATP mobility or a lack of Mg^{2+} coordination to the bound complex. Other than the addition of the lone ATP-binding site, the channel remained virtually unaltered with respect to the apo structure[10], having a 0.36-Å r.m.s. deviation.

Long, unbiased simulations do not reveal ATP permeation

In an effort to monitor ATP flux through the pore, we carried out long, multimicrosecond MD simulations, using the Anton special-purpose supercomputer[26]. We embedded the apo mVDAC1 structure[10] in a homogenous dimyristoylphosphatidylcholine (DMPC) bilayer with both termini facing the lower bath, corresponding to the IMS[27,28], and placed a single Mg^{2+}-coordinated ATP molecule in either the upper or the lower baths (5 mM effective concentration). We initiated several independent simulations lasting 0.6–4.8 µs from both configurations (**Supplementary Table 1**). In all cases, including simulations performed with an applied transmembrane potential, ATP entered the pore but failed to permeate the entire channel (**Supplementary Fig. 2a**,**c**). For the majority of each simulation, the phosphate tail of the ATP remained in contact with basic residues Lys12, Arg15 and Lys20 on the N-terminal α-helix, thus demonstrating the importance of the helix in forming favorable interactions with ATP, in agreement with previous studies[22–24] as well as with our crystallographic structure. Meanwhile, the A ring processively explored different portions of the channel including residues on the β-barrel wall opposite the helix (**Supplementary Fig. 2b**,**d** and **Supplementary Movie 1**).

Table 1 Data collection and refinement statistics

	mVDAC1–ATP
Data collection	
Space group	*C*121
Cell dimensions	
a, *b*, *c* (Å)	100.15, 58.37, 66.55
α, β, γ (°)	90.00, 99.25, 90.00
Resolution (Å)	50.00–2.28 (2.42–2.28)[a]
R_{merge}	0.03415 (0.6297)
$I / \sigma I$	23.13 (2.21)
Completeness (%)	99.3 (99.2)
Redundancy	3.64 (3.3)
Refinement	
Resolution (Å)	19.497–2.28
No. reflections	61,557
R_{work} / R_{free}	0.204 / 0.261
No. atoms	
Protein	2,212
Ligand / ion	143
Water	54
B factors	
Protein	70.40
Ligand / ion	125.70
Water	53.10
r.m.s. deviations	
Bond lengths (Å)	0.007
Bond angles (°)	1.109

The data set was measured from a single crystal.
[a]Values in parentheses are for highest-resolution shell.

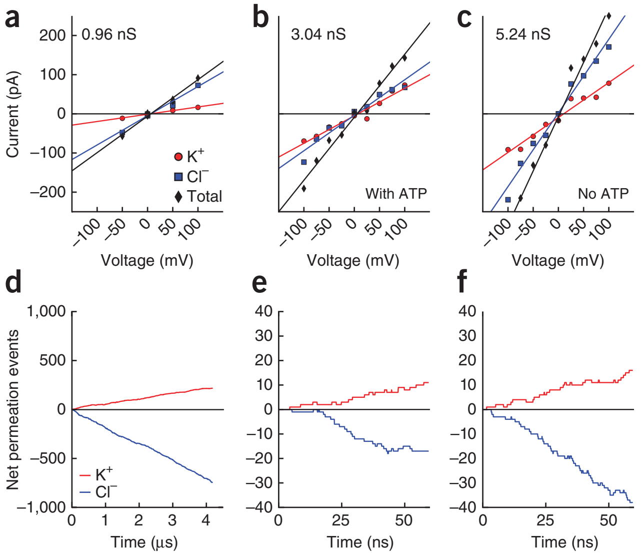

Figure 2 Simulated current-voltage curves and ion-permeation rates for mVDAC1. (**a**–**c**) Current-voltage curves under different ionic and ATP conditions. The current carried by K^+ (red) and by Cl^- (blue) and the total current, their sum (black), are shown. The lines are linear regressions of the respective data points, and they represent the current-voltage curves. **a** is compiled from 16.9 μs of aggregate simulation time carried out on a system in 142 mM KCl with ATP in the channel pore. **b** and **c** are compiled from shorter 60-ns simulations under high salt (900 mM KCl) with or without ATP in the pore, respectively. (**d**–**f**) The cumulative net number of channel-crossing events by Cl^- (blue traces) and K^+ (red traces), tracked over the time course of each simulation at +50 mV for physiological salt (142 mM) (**d**), high salt (900 mM) with ATP in the pore (**e**) and high salt (900 mM) with no ATP in the pore (**e**). Below each curve are the corresponding cumulative Cl^- and K^+ translocation events recorded at +50 mV (data not shown for other voltages).

mVDAC1 ion-conduction properties revealed from simulation

Although ATP does not cross the entire channel on the low-microsecond timescale, we observed hundreds of independent events of Cl^- and K^+ permeation from the Anton simulations. We constructed the current-voltage curve (**Fig. 2a**) by counting the total number of ion-translocation events per unit time in simulations carried out under various membrane potentials (**Fig. 2d**). After correcting for the simulated ion diffusion coefficients (Online Methods), the single-channel conductance was 0.96 nS in 142 mM KCl. Experimental estimates range from 0.45 to 0.58 nS in 100 mM KCl (ref. 15), which extrapolates to 0.64 to 0.83 nS in 142 mM KCl. Thus, our theoretical value is within 16% of the upper end of the experimental range, representing a dramatic improvement over our earlier estimate based on continuum electrodiffusion theory[16].

Next, we calculated the current-voltage curves with and without ATP in the channel to determine whether ATP occupancy influenced the channel's conduction properties (**Fig. 2b**,**c**). At each membrane potential, we ran a relatively short 60-ns simulation and increased the KCl concentration to ~0.9 M to increase the number of ion-translocation events. We also recorded the corresponding cumulative Cl^- and K^+ translocation events at +50 mV (**Fig. 2d**–**f**; data for other voltages not shown). The single-channel conductance values with and without ATP (determined from the slopes of the lines in **Fig. 2b**,**c**) are 3.04 and 5.24 nS, respectively. Thus, ATP reduced the conductance by 42%, results in excellent agreement with the experimental drop of 43% observed in single-channel currents under saturating ATP[23]. Moreover, the simulated conductance values are within 13% and 27% of the experimental range of 3.51–4.10 nS, which was extrapolated from 1 M (ref. 15) down to 0.9 M KCl. Interestingly, our simulations revealed that mVDAC1 has a moderate anion-to-cation selectivity of 4.0 in low KCl concentrations (on the basis of the ratio of the Cl^- to K^+ currents in **Fig. 2a**) and a much lower selectivity of 2.1 in high salt (**Fig. 2c**). Our calculations recapitulate the experimental finding that VDAC1 selectivity is ~5 (Cl^-/K^+) in physiological salt concentrations[29] and 1.7–1.9 under a 1.0–0.1 M KCl gradient[15]. Last, we found that ATP further reduced the anion selectivity of the channel by 40%, from 2.1 to 1.3, in high salt (**Fig. 2b**,**c**).

A Markov state model of ATP permeation

As an alternative approach to determine the ATP-permeation pathway, we used a computational method known as Markov state modeling[30,31]. We constructed a MSM of ATP movement through the channel by combining the results of 453 short simulations, each lasting 40–130 ns. We initiated these multiple simulations from an ensemble of ATP configurations located throughout the pore and bathing solutions, including a prerefined version of the crystal structure. In total, we generated 40 μs of aggregate simulation time resulting in 10 million snapshots saved at 4-ps intervals. We aligned all snapshots to a common reference structure by superposing the nonhydrogen atoms of the β-barrel. Next, we used the hybrid k-centers k-medoids algorithm within MSMBuilder[32] to cluster the positions of all ATP molecules within the pore domain of the channel with a 6.5-Å cluster radius, to result in 210 conformational states. The representative conformation for each state is known as the generator. We constructed the transition probability matrix, $P_{i,j}(\tau)$, for ATP starting in state i and moving to state j in lag time τ from the simulation data, using a maximum-likelihood reversible estimator[32]. From our analysis (**Supplementary Fig. 3**), we chose a lag time of 5 ns. To focus the computational effort on the slow transitions, we developed a framework for coupling an atomistic MSM with a continuum treatment of ATP diffusion in bulk solution, similar to previous work on proton transport by rotary ATPases[33]. Additional details concerning MSM construction can be found in Online Methods and **Supplementary Note**.

The individual simulations showed that ATP is highly mobile in the pore. In 20% of the simulations, the ATP moved >15 Å along the z axis (**Supplementary Fig. 4**) to result in either entry into the pore from the bulk or exit to the upper or lower baths (**Supplementary Movies 2**–**5**). We determined the equilibrium distribution of ATP in the channel from the transition probability matrix, and the probability of each of the 210 conformational states in the MSM is shown in **Figure 3a**. The dominant state had a modest occupancy of 16%, whereas occupancies of the next nine most populated states ranged from 2% to 6%. We observed considerable overlap between the most populated states in the MSM and the states most frequently visited by the longest Anton simulation (4.8 μs) (**Fig. 3a**), results lending strong validation to the MSM approach. Additionally, the Anton simulation showed that these stable ATP configurations interconvert on the microsecond timescale. However, the long simulation did not visit all MSM states, thus indicating superior coverage by the MSM simulations. The two most stable configurations showed ATP interacting with N-terminal α-helix residues Lys12, Arg15 and Lys20 (**Fig. 3b**). The next eight most populated states are structurally distinct, and this probably explains the weakness of ATP binding in the crystal structure. We note, in particular, that the ninth most populated state corresponds to a configuration in which the phosphate tail interacts with β-barrel residues Lys113 and Lys115 (**Fig. 3b**)—residues in the middle of a ten-residue stretch previously shown to interact with ATP via MS[22].

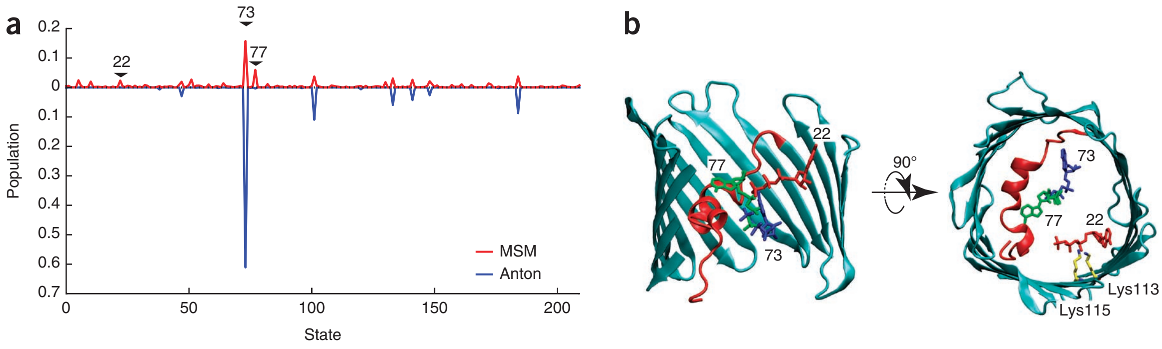

Figure 3 ATP adopts many conformations in the mVDAC1 pore. (**a**) Steady-state distribution of ATP in the pore domain, defined as -18 Å $\le z \le 20$ Å, calculated from the MSM (red). The most stable state (73) has 16% occupancy. The data from the longest Anton simulation (4.8 µs) is projected onto the MSM states (blue), and the relative probability of occupancy, determined from the time spent in each state, is plotted in the negative direction for clarity. (**b**) Structural diversity of the most stable ATP configurations. The generators for the first (73, blue), second (77, green) and ninth (22, red) most populated states are depicted. The phosphate tails of states 73 and 77 interact with basic residues (Lys12, Arg15 and Lys20) on the N-terminal helix, and the phosphate tail of state 22 interacts with Lys113 and Lys115 on the wall of the β-barrel.

Predicted ATP configurations agree with X-ray structure

On the basis of r.m.s. deviations between the X-ray structure and the generator molecule for each state in the MSM, the crystal structure most closely resembles the first (state 73, 5.80 Å), tenth (state 148, 5.31 Å) and nineteenth (state 58, 5.29 Å) most populated states. Thus, some of the most stable configurations from our model, including the most stable state, are the best matches to the experimental structure. One could argue that our MSM identified the X-ray structure as a stable site because we initiated simulations from this configuration; however, we believe that this is not the case, because the Anton simulations, which started with ATP in the bulk, also predicted state 73 to be extremely stable (**Fig. 3a**). To visualize the structural similarity between the simulations and experiment, we overlaid the closest ATP configuration from each state with the pose observed in the X-ray structure (**Fig. 4a**–**c**). Although the generator for state 58 has the smallest r.m.s. deviation to the X-ray structure, individual configurations belonging to state 148 (tenth most populated) and state 73 (first most populated) most closely match the X-ray structure, with r.m.s. deviations of 2.7 Å and 2.8 Å, respectively. Given the close structural similarity between all of these states, it is not surprising that the transition probability matrix indicates that ATP quickly interchanges between states 73 and 148, and slower exchange occurs between states 58 and 73 as well as states 58 and 148.

Mean first passage times indicate an open channel

The ATP flux through the channel can be computed from the MSM, thus allowing us to compare our simulated translocation rate with the experimental value. To do this, we calculated the mean first passage time (MFPT) between states, the reciprocal of which is the associated reaction rate[34]. We determined the MFPT from the transition probability matrix by solving the following set of linear equations (ref. 30 and **Supplementary Note**):

$$m_{i,j} = P_{i,j}\tau + \sum_{k \neq j} P_{i,k}(m_{k,j} + \tau)$$

where $m_{i,j}$ is the MFPT from state i to j. Our simulations predicted that the MFPT to move from the IMS to the cytoplasm is 32 µs (95% confidence interval 20–51 µs) under an ATP gradient of 5–0 mM applied with the continuum coupling model, whereas the reverse MFPT, with bathing concentrations switched, is 15 µs (95% confidence interval 10–22 µs). We generated the 95% confidence intervals by using a statistical bootstrapping procedure[35], as described in **Supplementary Note**. Although these rates should be identical on the basis of symmetry considerations, the MSM boundaries do not extend fully into the bulk, thus giving rise to slight asymmetries. The average rate based on these MFPTs is ~49,000 ATP/s, a result in excellent agreement with the experimental value of 50,000 ATP/s recorded from *Neurospora crassa* VDAC channels recorded in high ATP concentrations and extrapolated down to 5 mM ATP[12,13]. Thus, the ATP flux computed from the MSM again suggests that the crystallographic mVDAC1 structure represents the native open conformation.

Additional uncertainties in the computed rates arise from how the MSM is constructed. MSMs can be sensitive to the choice of cluster size and lag time. When the clusters are too large, states are composed of heterogeneous configurations, which may interchange more slowly than the lag time, thus leading to non-Markovian dynamics. However, if the cluster radius is too small, a large number of states are created, and it is difficult to adequately sample all of the interstate transition probabilities. State-splitting analysis indicated that over 90% of the states in our model at radius 6.5 Å exchange faster than the lag time (**Supplementary Fig. 5**), and removing these poorly connected states from our analysis did not affect the MFPTs. To further explore dependence on cluster size, we varied the cluster radius from 5 to 8 Å

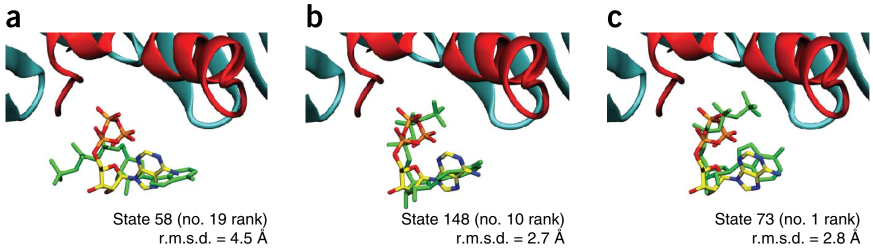

State 58 (no. 19 rank)
r.m.s.d. = 4.5 Å

State 148 (no. 10 rank)
r.m.s.d. = 2.7 Å

State 73 (no. 1 rank)
r.m.s.d. = 2.8 Å

Figure 4 Comparison between experimental ATP structure and MSM configurations. Overlay of the X-ray structure with ATP configurations taken from the top three most structurally similar MSM states: state 58 (nineteenth most populated; **a**), state 148 (tenth most populated; **b**) and state 73 (first most populated; **c**). In each panel, the ATP coloring scheme for the X-ray structure is as in **Figure 1**, and each structure from the MSM is solid green. The r.m.s. deviation (r.m.s.d.) between the experimentally determined ATP molecule and the representative MSM configuration is shown in each panel.

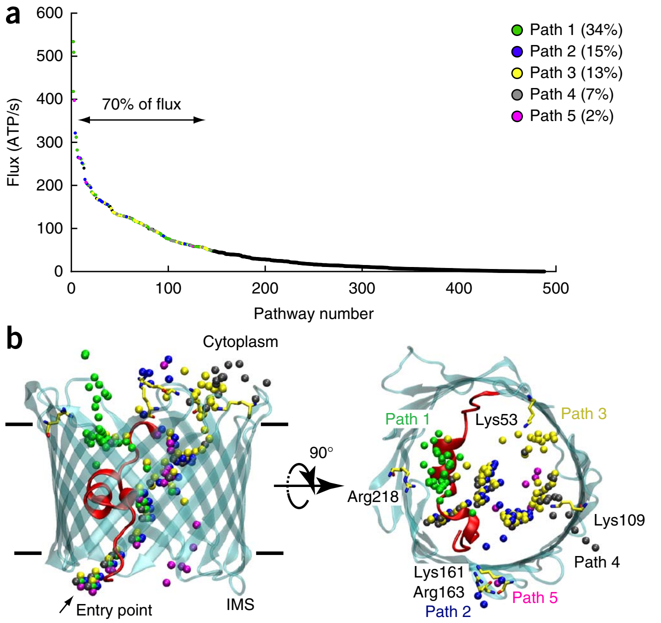

Figure 5 A high ATP flux is achieved through multiple distinct pathways. (**a**) Rank ordering of all distinct ATP-flux pathways through the channel from the IMS to the cytoplasm, as identified via transition path analysis. The highest-flux pathways giving rise to 70% of the total flux, identified and grouped into five primary paths on the basis of spatial analysis in **b**, are numbered according to their probability and color coded. (**b**) The γ-phosphate of ATP, plotted for all of the highest-flux pathways identified in **a**. The arrow indicates the common entry point for all paths.

and computed the corresponding MFPTs (**Supplementary Fig. 6e**). The IMS-to-cytoplasmic MFPTs ranged from 70 to 14 μs, whereas the reverse times ranged from 32 to 10 μs. For the reasons stated above, we believe that the values at 5 Å dramatically increase, owing to insufficient sampling, and we believe that the values at 8 Å are artificially low, owing to clustering of kinetically distinct configurations. We also varied the lag time to determine its influence on the kinetics. If τ is too short, the system will display non-Markovian dynamics, whereas increasing τ requires simulation data to be discarded, thus leading to poorer sampling. Our analysis revealed that the cytoplasm-to-IMS MFPT is remarkably constant over lag times from 5 to 30 ns, potentially because of good sampling of the bottleneck transition. However, the reverse time increases monotonically to 160 μs at τ equal 30 ns (**Supplementary Fig. 6f**), most probably owing to reduced sampling, which diminishes the quality of the MSM.

ATP permeates the VDAC via several distinct pathways

We determined the mechanism that ATP uses to pass from the IMS to the cytoplasm by applying transition path theory[36–38] to the MSM (**Fig. 5a**). Our analysis shows that permeation occurs via a number of distinct—and often intersecting—routes (**Fig. 5b**) involving 18 of the 28 pore-facing, basic residues (**Fig. 6a**–**c**). We visualized the top five paths, which account for ~70% of the total flux, by plotting the coordinates of the γ-phosphate for each state comprising a single path (**Fig. 5b**). In all pathways, ATP enters the channel at a single entry point through simultaneous interactions with the protein N terminus and Lys174 on the barrel wall. Along paths 1–4, Lys174 maintains an interaction with the γ-phosphate of ATP as the nucleotide is passed to Lys12 on the helix (**Fig. 6a**,**b**). ATP then interconverts among a series of stable states that involve interactions with helix residues Lys12, Arg15 and Lys20 (**Fig. 6a**,**b**). Along path 1, which carries 32% of the flux, ATP is released from the helix and transferred to Arg218 before exiting into the cytosol. Along paths 2–4, the phosphate tail breaks free from the N-terminal helix and moves across the channel to associate with Lys113 and Lys115 on the barrel wall. From there, paths 2, 3 and 4 diverge as ATP jumps to different basic residues lining the outer mouth of the channel (**Fig. 6b**). Path 3 is similar to the trajectory reported by Noskov and co-workers from their simulations of ATP in mVDAC1 (ref. 39). For paths 1–4, the rate-limiting step is dissociation of ATP from the α-helix. Along path 5, which is unique in that we saw no interactions between the ATP and the α-helix basic residues, translocation involves a sequential move along a series of lysine residues (Lys174, Lys119 and Lys96) on the β-barrel wall, opposite to the α-helix (**Fig. 6c**). The ATP then reaches Lys61, and the transition to Arg139, closer to the cytosol, is the rate-limiting step. From there, path 5 joins path 2 and exits via interactions with Lys161 and Arg163. Interestingly, although it accounts for only 2% of the calculated flux, path 5 displays one of the highest ATP-flux rates (**Fig. 5a**).

DISCUSSION

Our combined structural and computational studies indicate that ATP is loosely bound in the pore of mVDAC1, where it associates with basic residues on the N-terminal helix. The simulations reveal that the molecule is highly mobile in the pore, and this corroborates the weak binding suggested by the crystal structure. Despite this high degree of mobility, the long simulations on Anton failed to reveal a full permeation event on the timescale of the simulations, and instead the ATP remained affixed to the N-terminal helix. There was, nevertheless, very good agreement between the X-ray structure, the Anton simulations and the MSM analysis concerning the most stable configuration in the pore (**Fig. 4**). This agreement highlights the usefulness of

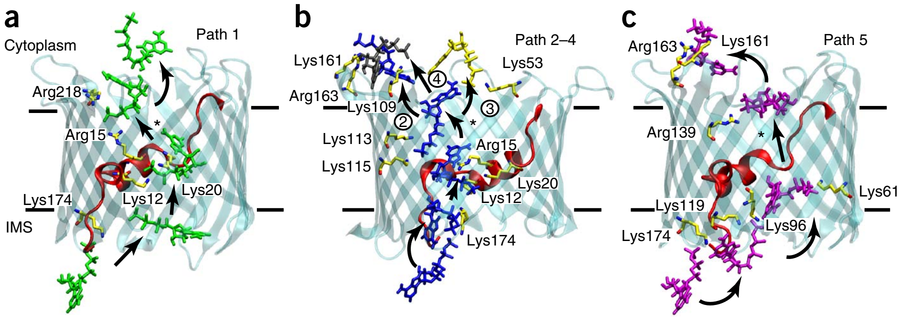

Figure 6 ATP permeates via a network of basic residues. (**a**) The highest-probability pathway (34%) from the IMS to the cytoplasm moves up and over the N-terminal helix. In all panels, arrows indicate the direction of flow from the IMS to the cytosol, and asterisks indicate the rate-limiting steps. For paths 1–4, the rate-limiting step is release from the patch of basic residues on the helix (Lys12, Arg15 and Lys20). Solid lines delineate the membrane boundaries. (**b**) Paths 2–4 (15%, 13% and 7% probability, respectively) share many states in common, except for the final state before escape to the cytoplasm. Numbers next to the final transition differentiate the paths. (**c**) Path 5 (2% probability) is the least-probable path, and it avoids the basic residues on the helix.

atomistic simulations, particularly MSMs, in identifying and ranking poses of small molecules in proteins, especially when interactions are too weak or too dynamic to easily be resolved via high-resolution structural techniques.

As mentioned already, a controversy still exists as to whether the published VDAC structures represent the native open state of the protein. Our simulations may help to resolve this issue, as they reliably predicted several biophysical properties of the open VDAC1 channel. First, the single-channel ion-conductance values computed from simulations in low salt and high salt were within the experimental range or 16–27% above them. Additionally, the drop in ion conductance resulting from the presence of ATP in the pore is in excellent agreement with experimental measurement[23]. Finally, our Anton simulations reproduced the increase in anion selectivity observed in experiments conducted in physiological salt concentrations[29]. Altogether, these observations support the hypothesis that the reported high-resolution structures of VDAC1 (refs. 9–11) represent its native open state. An important question is how the channel rearranges to close, and it has been hypothesized that this occurs via structural changes in the N-terminal helix[40–42]. Interestingly, our nearly 60 μs of simulations indicate that the helix is quite stable in the crystallized conformation (data not shown), and this might be expected because channel closure occurs on the timescale of seconds[29].

Our simulated ATP flux of 49,000 ATP/s closely matches the experimental estimates[12,13], but our parameter analysis based on results in **Supplementary Figure 6** places relatively conservative bounds on the rate between 100,000 and 6,000 ATP/s. Therefore, we caution against over interpreting the close correspondence of our prediction to experiment, especially given that there are additional sources of error stemming from both computational and experimental considerations. As with all simulations of rare events, finite sampling may introduce error into the calculated quantities. There are also errors associated with molecular force fields, and it has long been appreciated that charge-charge interactions are overly stabilized in several force fields[43–45], including the one used here[46]. We believe that a reduction in electrostatic interactions between the protein and ATP would reduce the dwell time in the channel to potentially result in faster permeation rates. With regard to experimental uncertainties, no flux studies have been carried out specifically in 5 mM ATP. The seminal work by Rostovtseva and Colombini calculated rates at 50 mM ATP and higher[12,13] and then interpolated back to 5 mM. Additionally, these experiments were carried out on mixtures of VDAC subtypes. Future studies performed on purified channels of a single subtype and carried out in 5 mM ATP are needed to provide a more quantitative comparison between theory and experiment.

More work must be done to determine the role of divalent cations, specifically Mg^{2+}, in the permeation process. It has been suggested that ATP permeates VDAC in the −4 charge state[12,23], on the basis of the observation that ATP flux is smaller than $citrate^{3-}$ flux, which in turn is smaller than the flux of $succinate^{2-}$ (ref. 12). Current noise analysis has also shown that small-molecule binding to VDACs increases with the charge on the molecule[47], and a recent NMR study concluded that ATP^{4-} binds more strongly in the absence of Mg^{2+} (ref. 25). This later observation may explain why we failed to observe Mg^{2+} bound to ATP in the structure. However, in our simulations we never observed Mg^{2+} to dissociate or change its coordination state with ATP; this implies that ATP permeates with a net −2 charge. Under physiological conditions, the majority of ATP is in complex with Mg^{2+} (ref. 48), and because Mg^{2+} also reduces ATP's binding affinity to the channel, it has been suggested that transport through VDACs occurs primarily in the Mg-ATP state[25]. Additional simulations in the absence of Mg^{2+} are needed to test this hypothesis.

From a more general point of view, our work demonstrates that the MSM approach to small-molecule transport bears the potential to overcome the current limitations of MD simulations in terms of providing a statistically valid description of slow processes. Here, we illuminated how ATP passes through the VDAC by 'hopping' along a series of weak binding sites (**Supplementary Movies 6** and **7**, composite movies of full crossing events via paths 1 and 2, respectively). The MSM revealed the myriad of pathways available for ATP permeation, and it provided their relative probabilities along with the occupancy of distinct ATP conformations in the channel. Such a rich statistical description is generally difficult to attain with individual, long MD simulations, but our work demonstrates that it is tractable with MSMs. MSM-generated steady-state distributions, along with transition pathway analysis, thus provide a new framework for studying ligand binding to membrane proteins, as well as ion or small-molecule permeation through channels and transporters.

METHODS

Methods and any associated references are available in the online version of the paper.

Accession codes. Coordinates and structure factors of mVDAC1 crystallized with ATP have been deposited in the Protein Data Bank under accession number 4C69.

Note: Any Supplementary Information and Source Data files are available in the online version of the paper.

ACKNOWLEDGMENTS

This work was supported by US National Science Foundation CAREER award MCB0845286 (M.G.) and US National Institutes of Health grants GM089740 (M.G.), T32-DK061296 (J.L.A.) and GM078844 (J.A.). O.P.C. was supported by an Andrew Mellon Predoctoral Fellowship from the University of Pittsburgh. J.-P.C. was supported by a Young International Fellowship from the Chinese Academy of Sciences. Simulations at the Texas Advanced Supercomputing Center were supported by grant MCB080011 (M.G.). The Anton special-purpose supercomputer was provided by the National Resource for Biomedical Supercomputing, the Pittsburgh Supercomputing Center and the Biomedical Technology Research Center for Multiscale Modeling of Biological Systems through grant P41GM103712-S1 from the US National Institutes of Health, and simulations on Anton were supported by grant PSCA00015P (M.G.). The Anton machine was generously made available by D.E. Shaw Research. We thank J.M. Rosenberg, K. Callenberg, F.V. Marcoline, Y. Sheng, H.Y. Wang and A. Vartanian for helpful discussions and R. Ujwal for contributions at the early stages of this work. We dedicate this work to the memory of Armand Vartanian, a colleague and friend.

AUTHOR CONTRIBUTIONS

A.P., J.-P.C. and J.A. collected and analyzed the diffraction data. O.P.C., J.L.A. and M.G. designed, conducted and analyzed the MD simulations. The manuscript was prepared by all authors.

COMPETING FINANCIAL INTERESTS

The authors declare no competing financial interests.

1. Törnroth-Horsefield, S. & Neutze, R. Opening and closing the metabolite gate. *Proc. Natl. Acad. Sci. USA* **105**, 19565–19566 (2008).
2. Rostovtseva, T.K. *et al.* Tubulin binding blocks mitochondrial voltage-dependent anion channel and regulates respiration. *Proc. Natl. Acad. Sci. USA* **105**, 18746–18751 (2008).
3. Schwarzer, C., Barnikol-Watanabe, S., Thinnes, F.P. & Hilschmann, N. Voltage-dependent anion-selective channel (VDAC) interacts with the dynein light chain Tctex1 and the heat-shock protein PBP74. *Int. J. Biochem. Cell Biol.* **34**, 1059–1070 (2002).

4. Shimizu, S., Narita, M. & Tsujimoto, Y. Bcl-2 family proteins regulate the release of apoptogenic cytochrome c by the mitochondrial channel VDAC. *Nature* **399**, 483–487 (1999).
5. Min, C.K. *et al.* Coupling of ryanodine receptor 2 and voltage-dependent anion channel 2 is essential for Ca^{2+} transfer from the sarcoplasmic reticulum to the mitochondria in the heart. *Biochem. J.* **447**, 371–379 (2012).
6. Geisler, S. *et al.* PINK1/Parkin-mediated mitophagy is dependent on VDAC1 and p62/SQSTM1. *Nat. Cell Biol.* **12**, 119–131 (2010).
7. Messina, A., Reina, S., Guarino, F. & De Pinto, V. VDAC isoforms in mammals. *Biochim. Biophys. Acta* **1818**, 1466–1476 (2012).
8. Colombini, M. VDAC: the channel at the interface between mitochondria and the cytosol. *Mol. Cell. Biochem.* **256–257**, 107–115 (2004).
9. Hiller, S. *et al.* Solution structure of the integral human membrane protein VDAC-1 in detergent micelles. *Science* **321**, 1206–1210 (2008).
10. Ujwal, R. *et al.* The crystal structure of mouse VDAC1 at 2.3 A resolution reveals mechanistic insights into metabolite gating. *Proc. Natl. Acad. Sci. USA* **105**, 17742–17747 (2008).
11. Bayrhuber, M. *et al.* Structure of the human voltage-dependent anion channel. *Proc. Natl. Acad. Sci. USA* **105**, 15370–15375 (2008).
12. Rostovtseva, T. & Colombini, M. VDAC channels mediate and gate the flow of ATP: implications for the regulation of mitochondrial function. *Biophys. J.* **72**, 1954–1962 (1997).
13. Rostovtseva, T. & Colombini, M. ATP flux is controlled by a voltage-gated channel from the mitochondrial outer membrane. *J. Biol. Chem.* **271**, 28006–28008 (1996).
14. Báthori, G., Csordas, G., Garcia-Perez, C., Davies, E. & Hajnoczky, G. Ca^{2+}-dependent control of the permeability properties of the mitochondrial outer membrane and voltage-dependent anion-selective channel (VDAC). *J. Biol. Chem.* **281**, 17347–17358 (2006).
15. Colombini, M. Voltage gating in the mitochondrial channel, VDAC. *J. Membr. Biol.* **111**, 103–111 (1989).
16. Choudhary, O.P. *et al.* The electrostatics of VDAC: implications for selectivity and gating. *J. Mol. Biol.* **396**, 580–592 (2010).
17. Rui, H., Lee, K.I., Pastor, R.W. & Im, W. Molecular dynamics studies of ion permeation in VDAC. *Biophys. J.* **100**, 602–610 (2011).
18. Colombini, M. The published 3D structure of the VDAC channel: native or not? *Trends Biochem. Sci.* **34**, 382–389 (2009).
19. Song, J., Midson, C., Blachly-Dyson, E., Forte, M. & Colombini, M. The topology of VDAC as probed by biotin modification. *J. Biol. Chem.* **273**, 24406–24413 (1998).
20. Hiller, S., Abramson, J., Mannella, C., Wagner, G. & Zeth, K. The 3D structures of VDAC represent a native conformation. *Trends Biochem. Sci.* **35**, 514–521 (2010).
21. Forte, M., Guy, H.R. & Mannella, C.A. Molecular genetics of the VDAC ion channel: structural model and sequence analysis. *J. Bioenerg. Biomembr.* **19**, 341–350 (1987).
22. Yehezkel, G., Hadad, N., Zaid, H., Sivan, S. & Shoshan-Barmatz, V. Nucleotide-binding sites in the voltage-dependent anion channel: characterization and localization. *J. Biol. Chem.* **281**, 5938–5946 (2006).
23. Rostovtseva, T.K. & Bezrukov, S.M. ATP transport through a single mitochondrial channel, VDAC, studied by current fluctuation analysis. *Biophys. J.* **74**, 2365–2373 (1998).
24. Rostovtseva, T.K., Komarov, A., Bezrukov, S.M. & Colombini, M. Dynamics of nucleotides in VDAC channels: structure-specific noise generation. *Biophys. J.* **82**, 193–205 (2002).
25. Villinger, S. *et al.* Nucleotide interactions of the human voltage-dependent anion channel. *J. Biol. Chem.* **289**, 13397–13406 (2014).
26. Shaw, D.E. *et al.* in *Proc. of the Conference on High Performance Computing Networking, Storage and Analysis* 1–11 (Institute of Electrical and Electronics Engineers, 2009).
27. Sheldon, K.L., Maldonado, E.N., Lemasters, J.J., Rostovtseva, T.K. & Bezrukov, S.M. Phosphorylation of voltage-dependent anion channel by serine/threonine kinases governs its interaction with tubulin. *PLoS ONE* **6**, e25539 (2011).
28. Tomasello, M.F., Guarino, F., Reina, S., Messina, A. & De Pinto, V. The voltage-dependent anion selective channel 1 (VDAC1) topography in the mitochondrial outer membrane as detected in intact cell. *PLoS ONE* **8**, e81522 (2013).
29. Colombini, M. VDAC structure, selectivity, and dynamics. *Biochim. Biophys. Acta* **1818**, 1457–1465 (2012).
30. Singhal, N., Snow, C.D. & Pande, V.S. Using path sampling to build better Markovian state models: predicting the folding rate and mechanism of a tryptophan zipper beta hairpin. *J. Chem. Phys.* **121**, 415–425 (2004).
31. Chodera, J.D., Singhal, N., Pande, V.S., Dill, K.A. & Swope, W.C. Automatic discovery of metastable states for the construction of Markov models of macromolecular conformational dynamics. *J. Chem. Phys.* **126**, 155101 (2007).
32. Beauchamp, K.A. *et al.* MSMBuilder2: modeling conformational dynamics at the picosecond to millisecond scale. *J. Chem. Theory Comput.* **7**, 3412–3419 (2011).
33. Elston, T., Wang, H. & Oster, G. Energy transduction in ATP synthase. *Nature* **391**, 510–513 (1998).
34. Reimann, P., Schmid, G.J. & Hanggi, P. Universal equivalence of mean first-passage time and Kramers rate. *Phys. Rev. E Stat. Phys. Plasmas Fluids Relat. Interdiscip. Topics* **60**, R1–R4 (1999).
35. Efron, B. & Tibshirani, R. Bootstrap methods for standard errors, confidence intervals, and other measures of statistical accuracy. *Stat. Sci.* **1**, 54–75 (1986).
36. Berezhkovskii, A., Hummer, G. & Szabo, A. Reactive flux and folding pathways in network models of coarse-grained protein dynamics. *J. Chem. Phys.* **130**, 205102 (2009).
37. Metzner, P., Schutte, C. & Vanden-Eijnden, E. Transition path theory for Markov jump processes. *Multiscale Model, Simul.* **7**, 1192–1219 (2009).
38. Noé, F., Schutte, C., Vanden-Eijnden, E., Reich, L. & Weikl, T.R. Constructing the equilibrium ensemble of folding pathways from short off-equilibrium simulations. *Proc. Natl. Acad. Sci. USA* **106**, 19011–19016 (2009).
39. Noskov, S.Y., Rostovtseva, T.K. & Bezrukov, S.M. ATP transport through VDAC and the VDAC-tubulin complex probed by equilibrium and nonequilibrium MD simulations. *Biochemistry* **52**, 9246–9256 (2013).
40. Guo, X.W. *et al.* Molecular design of the voltage-dependent, anion-selective channel in the mitochondrial outer membrane. *J. Struct. Biol.* **114**, 41–59 (1995).
41. Koppel, D.A. *et al.* Bacterial expression and characterization of the mitochondrial outer membrane channel: effects of N-terminal modifications. *J. Biol. Chem.* **273**, 13794–13800 (1998).
42. Colombini, M., Blachly-Dyson, E. & Forte, M. VDAC, a channel in the outer mitochondrial membrane. *Ion Channels* **4**, 169–202 (1996).
43. Duan, Y. *et al.* A point-charge force field for molecular mechanics simulations of proteins based on condensed-phase quantum mechanical calculations. *J. Comput. Chem.* **24**, 1999–2012 (2003).
44. Cerutti, D.S., Rice, J.E., Swope, W.C. & Case, D.A. Derivation of fixed partial charges for amino acids accommodating a specific water model and implicit polarization. *J. Phys. Chem. B* **117**, 2328–2338 (2013).
45. Debiec, K.T., Gronenborn, A.M. & Chong, L.T. Evaluating the strength of salt bridges: a comparison of current biomolecular force fields. *J. Phys. Chem. B* doi: 10.1021/jp500958r (5 April 2014).
46. Jensen, M.Ø. *et al.* Mechanism of voltage gating in potassium channels. *Science* **336**, 229–233 (2012).
47. Rostovtseva, T.K., Komarov, A., Bezrukov, S.M. & Colombini, M. VDAC channels differentiate between natural metabolites and synthetic molecules. *J. Membr. Biol.* **187**, 147–156 (2002).
48. Storer, A.C. & Cornish-Bowden, A. Concentration of $MgATP^{2-}$ and other ions in solution: calculation of the true concentrations of species present in mixtures of associating ions. *Biochem. J.* **159**, 1–5 (1976).

ONLINE METHODS

VDAC production and purification. Protein production and purification were performed largely as described previously[10]. In short, a histidine-tagged mVDAC1 was expressed in *Escherichia coli* M15 cells. Inclusion bodies were isolated, solubilized and purified on a Talon affinity column. mVDAC1 was subsequently refolded and further purified to homogeneity with a Superdex 75 size-exclusion column. The purified mVDAC1 sample was concentrated to 15 mg/ml in a solution containing 20 mM Tris-HCl, pH 8.0, 50 mM NaCl and 0.1% LDAO (protein solution).

Crystallization and diffraction data collection. mVDAC1 crystals were formed in bicelles with the hanging-drop vapor-diffusion technique by mixing the protein solution with a 35% bicelle solution in 4:1 ratio. The final concentration of the sample used for crystallization was 12 mg/ml in 7% bicelles. The protein/bicelle solution was mixed at a 1:1 ratio with mother liquor (18–20% MPD, 0.1 M Tris-HCl, pH 8.5, and 10% PEG 400) and set up over the mother liquor to allow for equilibration at 20 °C. Crystals appeared after 3–5 d. The resulting crystals were soaked in a solution containing all constituents of the protein and mother-liquor solutions with the addition of 50 mM ATP and 50 mM $MgCl_2$. The crystals were soaked for 1 h and subsequently transferred to a fresh solution containing the same components supplemented with 18% glycerol for 10 s and rapidly flash frozen in liquid nitrogen. The mVDAC1 crystals diffracted X-rays up to 2.3 Å. 180 frames of data were collected at the Advanced Light Source (Berkeley, California, USA) at beamline 5.0.2 with an oscillation angle of 1°, $T = 100$ K and $\lambda = 1.00$ Å.

Structure refinement. Diffraction data for ATP-soaked mVDAC1 were integrated and scaled between 19.51 and 2.3 Å with XDS and XSCALE[49]. PHENIX[50] was used for a rigid-body refinement against the previously solved mVDAC1 structure (PDB 3EMN)[10], devoid of water and lipid. No prominent positive density peaks that could be interpreted as ATP were observed in the pore of ATP-soaked mVDAC1 in the initial $F_o - F_c$ map; however, the $2F_o - F_c$ map clearly indicated the presence of extra density in the vicinity of the internal α-helix. Structural refinement of the model was carried out with PHENIX, and this was followed by iterative cycles of model building with Coot[51]. After thorough refinement of the polypeptide structure, CNS was used to calculate a Fourier difference map ($F_o^{\mathrm{ATP}} - F_o^{\mathrm{Native}}$) between the structure-factor amplitudes of the data set for ATP-soaked mVDAC1 and those of a native mVDAC1 data set. The differences in structure-factor amplitude were q-weighted to improve the signal-to-noise ratios of the Fourier difference maps[52,53] (**Supplementary Fig. 1a**). The two most prominent peaks of the ($F_o^{\mathrm{ATP}} - F_o^{\mathrm{Native}}$) map (5.1σ and 5.7σ) were found in the mVDAC1 pore, overlaying with the previously mentioned $2F_o - F_c$ peaks. Neither map provided a clear assignment for positioning ATP; therefore, annealed (annealing to 550 K, cooling steps of 25 K; 100 final steps of conjugate gradient minimization) omit map was calculated with CNS[54] (**Supplementary Fig. 1b**). The resulting map was interpretable and allowed for the fitting of an ATP molecule in the center of the pore. Two ATP orientations were possible on the basis of this map, and we refined each one of the orientations independently. The ATP orientation that was subsequently deposited and reported herein was chosen because it had a lower R_{free}, a higher real-space map correlation of the ATP molecule, and an increased number of contacts between the ATP and the protein. In the refined model, two atoms from the ATP molecule (O2γ and O1γ) directly contact protein atoms Lys12 Nζ and Lys20 Nζ at 2.3 and 3.3 Å, respectively (**Fig. 1**). The final ATP real-space map correlation is 0.8, and the average B factor is 214.1 Å^2 (**Supplementary Fig. 1c**). These values are consistent with weak binding between the ATP molecule and VDAC and suggest that ATP binds only transiently while passing through the channel. Overall data collection and refinement statistics are listed in **Table 1**. 95.8% of the final backbone dihedral angles were in the Ramachandran favored region and only 0.7% in the Ramachandran outlier region. Poor density was observed for residue Asn269 on the loop between β-strands 18 and 19.

Simulation setup. Models of VDAC were generated with the crystal structure of mVDAC1 (PDB 3EMN)[10]. The channel was centered at the origin, and the pore axis was aligned along the z axis, placing both N and C termini in the lower half of the simulation cell ($z < 0$). All ionizable groups were left in the dominant protonation state at pH 7.0, except residue Glu73, which was protonated because it faces lipid. A prerefined structure of the ATP molecule from the cocrystal was coordinated with a Mg^{2+} ion and used to initiate MD simulations. The ion was coordinate to the β- and γ-phosphate oxygen atoms of the ATP, in accordance with experiments on ATP in solution[55] and previous simulations[56]. As described in **Supplementary Note**, the prerefined ATP structure was placed in different regions of the channel to initiate additional MD simulations for MSM construction. To do this, the ATP-Mg^{2+} configuration was rigidly translated and/or rotated in the simulation box. Each model was then embedded in a DMPC lipid bilayer and solvated with a neutralizing quantity of KCl (140–150 mM, depending on the exact setup) with the CHARMM-GUI Membrane Builder[57]. A hexagonal unit cell was used, which consisted of 36,000 atoms. Simulations used the CHARMM additive-force-field C22 parameter set[58] with CMAP corrections[59] for the protein and the C36 parameter set for the lipids[60]. Parameters for the ATP were taken from the nucleic acids section of the C27 parameter set[61,62], and water molecules were represented by the TIP3P model[63].

Molecular-dynamics simulation details. MD simulations were performed on two different computational platforms. 453 simulations ranging in length from 40 to 130 ns were used to construct a MSM of ATP permeation through the VDAC, with resources at the Texas Advanced Computing Center. Additionally, a number of long trajectories ranging from 600 to 5,000 ns were generated with the Anton supercomputer[64] at the Pittsburgh Supercomputing Center (**Supplementary Table 1**). All of the simulations reported here share a common equilibration protocol, which was carried out with NAMD 2.7 (ref. 65). First, a 2,000-step energy minimization was performed with the conjugate gradient algorithm, during which all nonhydrogen atoms of the protein and ATP-Mg^{2+} were harmonically restrained to the preequilibration-model coordinates ($k = 5$ kcal/mol/Å^2). The system was then gradually heated to 303 K over 0.3 ns with the same set of external restraints used during the minimization. After thermalizing the system, the harmonic restraints were gradually removed over 2 ns. During each of these steps, an external force was applied to all water molecules outside of the hydrated channel to prevent them from entering the protein-membrane interface or penetrating the hydrophobic core of the membrane. For equilibration and production runs, the temperature was controlled through Langevin dynamics with a damping coefficient of 5 ps^{-1}. A constant pressure of 1 atm was maintained with a Nosé-Hoover Langevin piston barostat with a piston period and decay timescale of 200 fs and 100 fs, respectively. The three orthogonal dimensions of the periodic cell were allowed to fluctuate independently during the simulation. The dynamics were propagated with a multiple time-stepping algorithm in which bonded and short-range nonbonded interactions were evaluated every 2 fs, and long-range electrostatic interactions every 4 fs. Short-range nonbonded interactions were truncated smoothly with a spherical cutoff radius of 10 Å and a switching distance of 8 Å. Long-range electrostatic interactions were calculated with the particle mesh Ewald (PME) method, with a grid density of approximately 1 Å^3. All hydrogen atom–heavy atom bond lengths were constrained with the SHAKE algorithm[66]. Subsequent production simulations used to construct the MSM used the same parameters, but without biasing forces. Simulations performed on Anton were prepared as above except with a larger rectangular box containing 57,000 atoms. The equilibration protocol above was then extended 20 ns in NAMD followed by an additional 40 ns with the simulation package Desmond version 2.2.9.1 (ref. 67). In Desmond, the dynamics were propagated with constant temperature (312 K) and pressure (1 atm) with the Martyna-Tobias-Klein (MTK) method[68], with a coupling constant of 2.0 ps^{-1} for the thermostat and barostat and a 2-fs time step. The barostat was isotropic in x and y but independent in z. Hydrogen positions were constrained with the M-SHAKE algorithm with a tolerance of 1.0×10^{-8}. Long-range electrostatics were computed with the PME method with 90 Fourier mesh points along each cell axis. Nonbonded and electrostatic interactions were cut off at a radius of 10 Å. Production simulations on Anton were initiated from the final snapshot of the corresponding equilibration runs on Desmond. A multiple-timestep integration scheme was used to propagate the dynamics on the basis of a Nosé-Hoover themostat, and the MTK method was used to maintain constant pressure. Long-range electrostatic interactions were calculated with the k-space Gaussian Split Ewald method[69]. All simulations involving a membrane potential were carried out as in ref. 70. Briefly, a membrane potential, V, across the lipid bilayer was imposed by application of a force, $F_i = q_i E$, perpendicular to the plane of the membrane to every atom i, proportional to its partial charge q_i.

doi:10.1038/nsmb.2841

The constant electric field, E, was chosen to give the desired membrane potential according to $V = EL$, where L is the length of the periodic cell in the z dimension. Details on Markov state modeling can be found in **Supplementary Note**.

Current-voltage and selectivity analysis. The selectivity and conductance of mVDAC1 were determined by calculation of the current-voltage relationship for the channel under varying applied electric fields. We determined the cumulative number of K^+ and Cl^- permeation events from the trajectories generated on Anton, as well as those from an additional data set generated on Stampede, but distinct from the trajectories used to build the MSM of ATP permeation. The Anton simulations were carried out in 142 mM KCl, and the Stampede simulations were carried out in ~0.9 M KCl. A particular ion was required to move from one bulk region of the simulation box to the other, through the channel, to count as a complete permeation event. At each voltage, the current contributed by each species of mobile ion was determined via a linear regression of the net ion crossing events as a function of the simulation time. The total current was simply the sum of the net K^+ current minus the net Cl^- current. The raw conductance was taken as the slope of the total least-squares linear regression to the individual current values plotted at each voltage[71], and these fits are shown in **Figure 2a**–**c**. The same fitting procedure was used to determine the slopes of the K^+ and Cl^- currents, and the selectivity was determined from the ratio of the fitted slopes.

The final reported channel conductance for each system was then determined by multiplying the raw conductance values (0.94, 1.61, and 2.77 nS for **Fig. 2a**–**c**, respectively) by a correction factor that accounted for simulated errors in the ion diffusion coefficient values. Although the diffusion coefficients of Cl^- and K^+ calculated from our long simulations on the Anton supercomputer (1.97×10^{-5} cm^2/s and 1.63×10^{-5} cm^2/s, respectively) are in good agreement with experimental values (2.02×10^{-5} cm^2/s and 1.96×10^{-5} cm^2/s, respectively[72]), values obtained for our simulations run on Stampede with NAMD are notably lower. In the simulations lacking ATP, the diffusion constants were 1.07×10^{-5} cm^2/s and 0.70×10^{-5} cm^2/s for Cl^- and K^+, respectively. The discrepancy most probably arises from our use of different temperature-coupling schemes and their parameterization used by NAMD and Anton. Temperature-coupling protocols can perturb the kinetics of a MD simulation in a systematic way, and Langevin thermostats, like the one used in the NAMD simulations, can nontrivially slow the diffusion of mobile species[73]. Because the majority of the current is carried by the Cl^- ions, we correct for this effect by scaling all of our calculated conductance values by the ratio of the experimental to simulated Cl^- diffusion coefficients. Specifically, conductance values from Anton simulations are scaled by 2.02/1.97, and all conductance values from Stampede simulations are scaled by 2.02/1.07, the value determined in ATP-free conditions.

49. Kabsch, W. Automatic processing of rotation diffraction data from crystals of initially unknown symmetry and cell constants. *J. Appl. Crystallogr.* **26**, 795–800 (1993).
50. Adams, P.D. *et al.* PHENIX: a comprehensive Python-based system for macromolecular structure solution. *Acta Crystallogr. D Biol. Crystallogr.* **66**, 213–221 (2010).
51. Emsley, P. & Cowtan, K. Coot: model-building tools for molecular graphics. *Acta Crystallogr. D Biol. Crystallogr.* **60**, 2126–2132 (2004).
52. Ursby, T. & Bourgeois, D. Improved estimation of structure-factor difference amplitudes from poorly accurate data. *Acta Crystallogr. A* **53**, 564–575 (1997).
53. Colletier, J.P. *et al.* Use of a 'caged' analogue to study the traffic of choline within acetylcholinesterase by kinetic crystallography. *Acta Crystallogr. D Biol. Crystallogr.* **63**, 1115–1128 (2007).
54. Brünger, A.T. *et al.* Crystallography & NMR system: a new software suite for macromolecular structure determination. *Acta Crystallogr. D Biol. Crystallogr.* **54**, 905–921 (1998).
55. Cohn, M. & Hughes, T.R. Jr. Nuclear magnetic resonance spectra of adenosine di- and triphosphate: II. Effect of complexing with divalent metal ions. *J. Biol. Chem.* **237**, 176–181 (1962).
56. Liao, J.C., Sun, S., Chandler, D. & Oster, G. The conformational states of Mg.ATP in water. *Eur. Biophys. J.* **33**, 29–37 (2004).
57. Jo, S., Kim, T. & Im, W. Automated builder and database of protein/membrane complexes for molecular dynamics simulations. *PLoS ONE* **2**, e880 (2007).
58. MacKerell, A.D. *et al.* All-atom empirical potential for molecular modeling and dynamics studies of proteins. *J. Phys. Chem. B* **102**, 3586–3616 (1998).
59. MacKerell, A.D. Jr., Feig, M. & Brooks, C.L. III. Improved treatment of the protein backbone in empirical force fields. *J. Am. Chem. Soc.* **126**, 698–699 (2004).
60. Klauda, J.B. *et al.* Update of the CHARMM all-atom additive force field for lipids: validation on six lipid types. *J. Phys. Chem. B* **114**, 7830–7843 (2010).
61. Foloppe, N. & MacKerell, A.D. Jr. All-atom empirical force field for nucleic acids: I. Parameter optimization based on small molecule and condensed phase macromolecular target data. *J. Comput. Chem.* **21**, 86–104 (2000).
62. Pavelites, J.J., Gao, J., Bash, P.A. & Mackerell, A.D. A molecular mechanics force field for NAD$^+$ NADH, and the pyrophosphate groups of nucleotides. *J. Comput. Chem.* **18**, 221–239 (1997).
63. Jorgensen, W.L., Chandrasekhar, J., Madura, J.D., Impey, R.W. & Klein, M.L. Comparison of simple potential functions for simulating liquid water. *J. Chem. Phys.* **79**, 926–935 (1983).
64. Shaw, D.E. *et al.* Anton, a special-purpose machine for molecular dynamics simulation. *Commun. ACM* **51**, 91–97 (2008).
65. Phillips, J.C. *et al.* Scalable molecular dynamics with NAMD. *J. Comput. Chem.* **26**, 1781–1802 (2005).
66. Ryckaert, J.P., Ciccotti, G. & Berendsen, H.J.C. Numerical integration of the cartesian equations of motion of a system with constraints: molecular dynamics of *n*-alkanes. *J. Comput. Phys.* **23**, 327–341 (1977).
67. Bowers, K.J. et al. in *Proc. of the 2006 ACM/IEEE Conference on Supercomputing* 43–43 (Institute of Electrical and Electronics Engineers, 2006).
68. Martyna, G.J., Tobias, D.J. & Klein, M.L. Constant pressure molecular dynamics algorithms. *J. Chem. Phys.* **101**, 4177–4189 (1994).
69. Shan, Y., Klepeis, J.L., Eastwood, M.P., Dror, R.O. & Shaw, D.E. Gaussian split Ewald: a fast Ewald mesh method for molecular simulation. *J. Chem. Phys.* **122**, 54101 (2005).
70. Gumbart, J., Khalili-Araghi, F., Sotomayor, M. & Roux, B. Constant electric field simulations of the membrane potential illustrated with simple systems. *Biochim. Biophys. Acta* **1818**, 294–302 (2012).
71. Ivezic, Z., Connolly, A., VanderPlas, J. & Gray, A. *Statistics, Data Mining, and Machine Learning in Astronomy* (Princeton University Press, 2013).
72. Hille, B. *Ion channels of excitable membranes* (Sinauer, Sunderland, Massachusetts, USA, 2001).
73. Basconi, J.E. & Shirts, M.R. Effects of temperature control algorithms on transport properties and kinetics in molecular dynamics simulations. *J. Chem. Theory Comput.* **9**, 2887–2899 (2013).